Toward Efficient Tandem Electroreduction of CO_2 to Methanol using Anodised Titanium

Wei Jie Teh[a], Oriol Piqué[b], Qi Hang Low[a], Weihan Zhu[a], Federico Calle-Vallejo[b,*], Boon Siang Yeo[a,*]

[a.] Department of Chemistry, National University of Singapore, 3 Science Drive 3, Singapore 117543 and Solar Energy Research Institute of Singapore, National University of Singapore, 7 Engineering Drive 1, Singapore 117574.

[b.] Department of Materials Science and Chemical Physics & Institute of Theoretical and Computational Chemistry (IQTCUB), University of Barcelona, Martí i Franquès 1, 08028 Barcelona, Spain.

* To whom correspondence should be addressed: BSY (Email: chmyeos@nus.edu.sg) or FCV (Email: f.calle.vallejo@ub.edu).

Abstract

The electroreduction of CO_2 (CO_2RR) using renewable electricity is an appealing route to synthesize methanol (CH_3OH), a valuable C_1 feedstock and fuel. Unfortunately, there are still no workhorse electrocatalysts with suitable activity and selectivity for this reaction. Currently, formic acid ($HCOOH$), CO and methane are the most common C_1 products. Since multi-electron electrocatalytic reactions can be severely affected by adsorption-energy scaling relations, a tandem process likely offers higher efficiency. We, therefore, strategize to reduce CO_2 to $HCOOH$, and then reduce $HCOOH$ to CH_3OH. While the former step can be

accomplished with ease using post-transition metals, the latter is extremely difficult due to the electrochemical inertness of HCOOH. Herein, we develop anodised titanium catalysts containing Ti^{3+} sites and oxygen vacancies (termed as TOVs), which can reduce HCOOH to CH_3OH with a remarkable Faradaic efficiency of 12.6 % and a partial current density of -2 mA/cm^2 at -1.0 V vs the reversible hydrogen electrode (RHE). Using electron paramagnetic resonance spectroscopy and cyclic voltammetry, we show that the population of TOVs on the catalyst is positively correlated with CH_3OH production. DFT calculations identify TOVs at defects as the active sites, in a vacancy-filling pathway mediated by $*H_2COOH$. We further provide holistic screening guidelines based on the $*HCOOH$ and $*H_2COOH$ binding energies, alongside TOV formation energies. These can open the path for the high-throughput, automated design of catalysts for CH_3OH synthesis from tandem CO_2 electrolysis.

Keywords: formic acid reduction, electrocatalysis, oxygen vacancies, density functional theory, methanol.

1. Introduction

Methanol (CH_3OH) is a major transportation fuel and chemical feedstock, and 95 million tonnes of it are produced worldwide annually.[1] Currently, CH_3OH is produced industrially by reacting syngas (CO and H_2) over copper-zinc oxide catalysts. However, high temperatures and pressures are required in synthesising CH_3OH (200–300 ºC and 50–100 bar)[2] and the syngas reactant (*via* steam reforming of natural gas at ~850 ºC and ~30 bar over a nickel catalyst).[3] Overall, the typical industrial production of one kg of CH_3OH leads to a net positive emission of ~0.5 kg of CO_2.[4] For these reasons, a greener pathway toward CH_3OH production is needed.

A sustainable route to CH_3OH production is through the electrochemical CO_2 reduction reaction (CO_2RR), which can be powered by renewable electricity. However, there are, to date, no workhorse electrocatalysts which can directly reduce CO_2 to CH_3OH with industrially-relevant activity, selectivity and stability.[5,6] To overcome this obstacle, one can resort to a tandem strategy in which CO_2 is first reduced to HCOOH, and the latter is then reduced to CH_3OH. The first step has already been achieved with Faradaic efficiencies (FEs) for HCOOH production close to 100 % using catalysts based on post-transition metals such as tin,[7] indium,[8] and lead.[9]

The second step, namely, formic acid reduction (FAR) to CH_3OH (HCOOH + $4H^+$ + $4e^-$ → CH_3OH + H_2O, E^0 = +0.11 V vs. RHE),[10] is more challenging because of the electrochemical inertness of HCOOH. This is caused by the low electrophilicity of the carbonyl carbon that is part of a conjugated carboxylic acid functional group.[11] Thus, while ketones and aldehydes formed from CO_2RR can be further reduced to give alcohols,[12,13] HCOOH and other carboxylic acids are dead-end CO_2RR products on transition metal electrodes.[14]

Early efforts to reduce formic acid to CH_3OH were from Russell et al., whose team employed an electro-etched Sn catalyst.[15] While the reported Faradaic efficiency for CH_3OH

(FE$_{CH3OH}$) was nearly 100 %, its partial current density (j_{CH3OH}) was 3.6 µA/cm^2, which limits the practicality of the process. Kyriacou et al. found that HCOOH could be reduced to CH$_3$OH on a Cr foil catalyst (FE$_{CH3OH}$ = 37.4 %) in 85 % phosphoric acid electrolyte at 80 °C.[16] Adegoke et al. reported a FE$_{CH3OH}$ of 11.9 % for FAR on In$_2$O$_3$ nanoparticles at an applied cell voltage of 3.5 V in a two-electrode electrolyser.[17] While FAR activity has been observed in these scattered reports, the key active sites and mechanistic pathways are still unclear. These voids of knowledge severely limit research efforts to improve FAR to CH$_3$OH.

Recently, it was shown that the anatase phase of TiO$_2$ could electroreduce non-aromatic carboxylic acids, such as oxalic acid, to their corresponding aldehydes and finally to alcohols.[11] Through adsorption and density functional theory (DFT) studies, it was proposed that significant interaction of the carboxylic acid with the catalyst surface is necessary for electron transfer from the electrode to the LUMO of the molecule. Interestingly, HCOOH could not be reduced. Thus, new approaches capitalizing on this finding are clearly needed. Herein, we put forth another strategy to improve the electroreduction of carboxylic acids by using the Ti^{3+} and oxygen vacancy sites of TiO$_2$ (hereon denoted as TOVs), which can be created by applying a negative voltage on the material. We propose that TOVs aid in C-O bond scission by directly stripping O atoms from the reactants, giving rise to new pathways for the reduction of carboxylic acids. In this respect, TiO$_2$ is an appealing catalyst for C-O scissions, as the strong Ti-O bond lowers the activation energy of C-O bond cleavage.[18]

On the basis of the above discussion, we anodised titanium (Ti$_{an}$), an earth-abundant and relatively inexpensive element, so as to introduce TOVs to its surface. Ti$_{an}$ exhibits significant electrocatalytic activity for FAR to CH$_3$OH. We quantitatively assess the impact of varying the amount of TOVs on Ti$_{an}$ for CH$_3$OH production using electron paramagnetic resonance and cyclic voltammetry. These experimental findings, coupled with DFT calculations, allow us to elucidate the catalytic pathway for FAR to CH$_3$OH, determine that the

critical active sites are the TOVs, and provide quantitative guidelines for the future enhancement of FAR catalysts.

2. Results and discussion

2.1. Formation and characterisation of Ti^{3+} and oxygen vacancies on anodised Ti

Our strategy for forming TOVs is as follows: Ti discs were first anodised at +0.25 A/cm^2 in 0.2 M KCl solution for 3 min ($Ti_{an, 3\ min}$). Scanning electron microscopy (SEM) revealed that the $Ti_{an, 3\ min}$ catalyst surface consisted of particles with grooves of 1.5 - 2 µm long (Figure 1a). The discs were then reduced in-situ during FAR at a representative potential of −1.0 V vs RHE to produce TOVs (all potentials reported hereafter are referenced to the RHE). No significant changes to the catalyst surface after FAR could be discerned by SEM (Figure 1b).

X-ray photoelectron spectroscopy (XPS) of a freshly prepared $Ti_{an, 3\ min}$ catalyst (Figures 1c–1f) revealed that the main surface Ti species is Ti^{4+} (in TiO_2), as indicated by its $2p_{3/2}$ and $2p_{1/2}$ peaks at 458.7 eV and 464.5 eV, respectively.[19] O_{1s} peaks observed at 530.4 eV and 531.6 eV correspond to oxygen in TiO_2 (Ti-O) and surface hydroxyl groups (Ti-OH), respectively.[20] No changes in the XPS spectra were observed for the $Ti_{an, 3\ min}$ catalyst after it had been used for FAR at −1.0 V (Figures S1a–1c). However, XPS of its subsurface, exposed after 30-min Ar^+ ion etching, revealed peaks at 457.6 eV and 463.4 eV. These can be respectively assigned to the $2p_{3/2}$ and $2p_{1/2}$ peaks of Ti^{3+}, indicating the reduction of Ti^{4+} to TOVs during FAR.[21] We note here that TOVs were not observed on the surface of the pre-etched catalyst, as they would have rapidly oxidised to Ti^{4+} after electrolysis and during sample transfer.[22] Ultraviolet-visible diffuse reflectance spectroscopy of Ti_{an} after FAR further confirmed the presence of Ti^{3+}, by its characteristic absorption peak between 400 to 800 nm (Figure S2).[23]
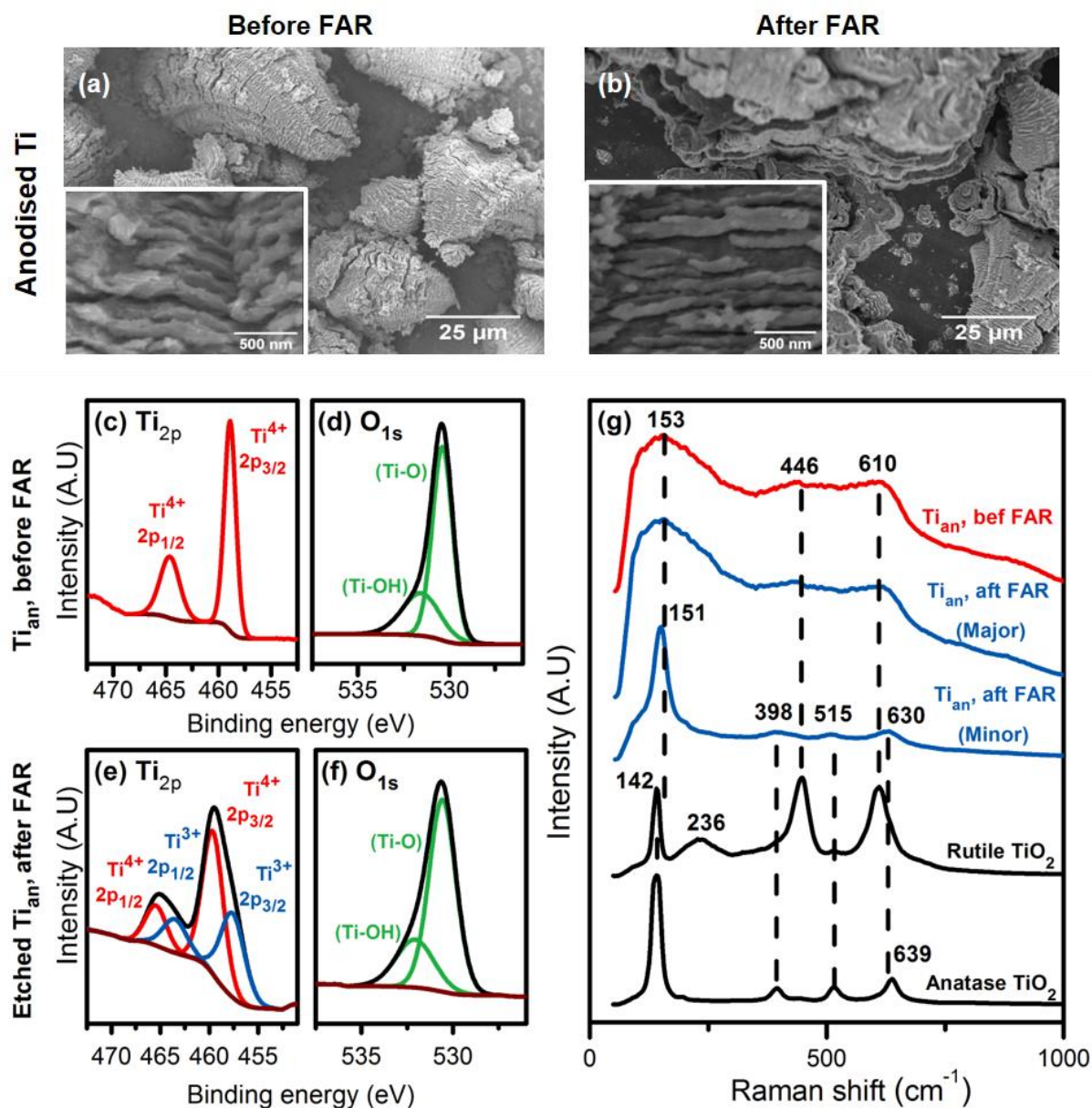
Before FAR   **After FAR**

(a) Anodised Ti   500 nm   25 µm

(b)   500 nm   25 µm

(c) Ti$_{2p}$ Ti$_{an}$, before FAR

Ti^{4+} 2p$_{3/2}$

Ti^{4+} 2p$_{1/2}$

470 465 460 455
Binding energy (eV)

(d) O$_{1s}$

(Ti-O)

(Ti-OH)

535 530
Binding energy (eV)

(e) Ti$_{2p}$ Etched Ti$_{an}$, after FAR

Ti^{4+} 2p$_{3/2}$
Ti^{3+} 2p$_{1/2}$
Ti^{4+} 2p$_{1/2}$
Ti^{3+} 2p$_{3/2}$

470 465 460 455
Binding energy (eV)

(f) O$_{1s}$

(Ti-O)

(Ti-OH)

535 530
Binding energy (eV)

(g) 153   446   610   Ti$_{an}$, bef FAR

151   Ti$_{an}$, aft FAR (Major)

398 | 515 | 630   Ti$_{an}$, aft FAR (Minor)

142 236   Rutile TiO$_2$

639   Anatase TiO$_2$

0   500   1000
Raman shift (cm^{-1})

Figure 1. Characterisation of Ti anodised for 3 min in 0.2 M KCl (Ti$_{an, 3 min}$). (a) SEM images of Ti$_{an, 3 min}$ before FAR and (b) after FAR at –1.0 V vs RHE. The insets are the magnified images of Ti$_{an}$ before and after FAR. XPS analyses of (c)-(d): Ti$_{an, 3 min}$ before FAR, (e)-(f): Ti$_{an, 3 min}$ after FAR at –1.0 V vs RHE, after its surface was etched with an Ar$^+$ ion beam. (g) Raman spectra of TiO$_2$ standards, and Ti$_{an, 3 min}$ before and after FAR at –1.0 V vs RHE. The peak intensities in the Raman spectra of Ti$_{an, 3 min}$ before FAR and Ti$_{an, 3 min}$ after FAR (Major) were ~5× smaller than those of the Raman spectrum of Ti$_{an, 3 min}$ after FAR (Minor), and were rescaled here for clarity.

X-ray diffraction (XRD) of the Ti$_{an, 3 min}$ catalyst before and after FAR at –1.0 V showed no well-defined crystalline anatase or rutile TiO$_2$ XRD peaks, which suggests that it was XRD-amorphous (Figure S3). In contrast, Raman spectroscopy of the Ti$_{an, 3 min}$ catalyst revealed TiO$_2$ peaks (Figure 1g, Table S4). Before FAR, Raman bands at 153, 446 and 610 cm^{-1} corresponding to rutile TiO$_2$ were recorded.[24] These bands were broadened and shifted,

6

indicating lattice disorder and defects in $Ti_{an, \, 3 \, min}$.[19] Note that rutile TiO_2 was detected by Raman spectroscopy, but not by XRD because of the absence of long-range order in the $Ti_{an, \, 3 \, min}$ catalyst.[25,26]

The crystallography of the $Ti_{an, \, 3 \, min}$ catalyst remained largely unchanged after FAR at −1.0 V (blue-coloured Raman spectrum in Figure 1g; denoted as 'major'). However, we also observed Raman bands at 151, 398, 515 and 630 cm^{-1} on a few spots of the $Ti_{an, \, 3 \, min}$ catalyst (spectrum denoted as 'minor'). These bands can be ascribed to anatase TiO_2.[24] These results suggest that a portion of amorphous $Ti_{an, \, 3 \, min}$ crystallised to anatase TiO_2 during FAR, which is in agreement with previous works on the electrochemical behaviour of amorphous TiO_2 nanotubes in water.[27,28]

2.2. Electrocatalytic activity of Ti_{an} for FAR to CH_3OH

The FAR activities of Ti_{an} were evaluated using a three-electrode setup, with a Ag/AgCl (saturated KCl) and graphite rod respectively employed as the reference and counter electrodes. Chronoamperometry was performed in 0.1 M K_2SO_4 electrolyte + 0.5 M HCOOH (pH 2.6) at potentials from −0.90 to −1.05 V, using $Ti_{an, \, 3 \, min}$ catalysts. HCOOH was reduced to CH_3OH with an optimal FE_{CH3OH} of 12.6 % and a j_{CH3OH} of −2 mA/cm^2 at −1.0 V (Figure 2a, Table S5, ^{1}H NMR and gas chromatography data in Figure S4; all reported current densities were normalized to the geometric surface area of the electrode). No CH_3OH was detected in the absence of electrochemical potentials, which shows that it was generated electrochemically.

Methane (CH_4) and formaldehyde (CH_2O) were detected as minor FAR products (FE_{CH4} = 1.4 % and FE_{CH2O} = 0.1 % at −1.0 V); hydrogen gas from the parasitic hydrogen evolution reaction (HER) formed the bulk of the remaining products. To assess if CH_4 is a product of either CH_3OH or CH_2O reduction, we reduced 5 mM of the latter two molecules in 0.1 M K_2SO_4 at −1.0 V on a $Ti_{an, \, 3 \, min}$ catalyst (Table S6). No CH_4 was detected, indicating that it was formed from the reduction of HCOOH. While CH_2O is a known precursor of CH_3OH,

7

only small amounts of CH_3OH were obtained during CH_2O electrolysis.[6] This observation will be further explained in Section 2.4.
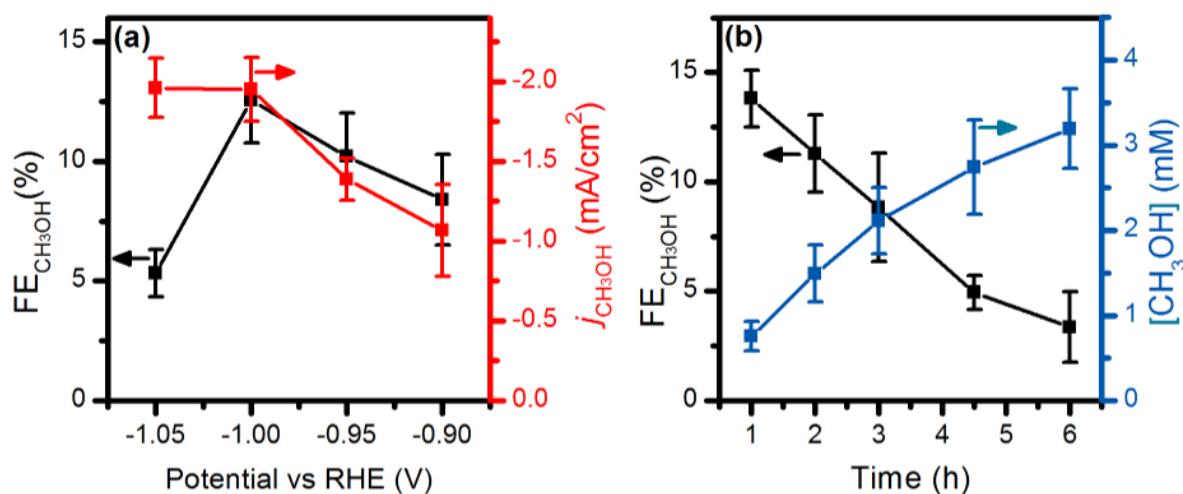

Figure 2. Formic acid reduction (FAR) using $Ti_{an, 3\ min}$ electrocatalysts in 0.1 M K_2SO_4 electrolyte with 0.5 M HCOOH added (pH ~2.6). (a) Faradaic efficiency, FE (%) and partial current density, j (mA/cm^2) of CH_3OH obtained during 60 min FAR at different applied potentials. (b) FE (%) and accumulated concentrations (mM) of CH_3OH production from FAR for 6 h at –1.0 V vs RHE. (Arrows are included to guide the eye to the respective graph axes.)

Trace amounts (3 – 14 ppm) of carbon monoxide (CO) were also detected during FAR. They were likely formed from HCOOH dehydration over the TOVs (Table S7), in agreement with previous works by Iwasawa et al., where in-situ experimental and theoretical studies were used to model HCOOH dehydration to CO on TOVs.[29,30]

Catalytic stability was assessed by performing a 6 h HCOOH electrolysis on $Ti_{an, 3\ min}$ at –1.0 V (Figure 2b, Section S3.4). CH_3OH was formed throughout the entire period, although its rate of formation decreased from 11.6 to 4.6 μmol h^{-1}cm^{-2}. We also noted that the FE_{CH3OH} decreased from 13.8 to 3.4 %. Based on the Pourbaix diagram of TiO_2, dissolution of TiO_2 to Ti^{2+} can occur at pH 2.6 and –1.0 V (or –1.15 V vs. SHE).[31] We thus hypothesise that the decrease in CH_3OH activity and selectivity is due to catalyst layer dissolution of Ti_{an} during prolonged electrolysis. This is verified by SEM imaging of the catalysts which showed loss of Ti_{an} after 6 h FAR. Inductively coupled plasma-optical emission spectrometry (ICP-OES) analysis also detected 8.6 ppm of Ti in the electrolyte after 6 h FAR at –1.0 V. This corresponds to 0.103 mg of Ti, which is a ~7 % loss of Ti_{an} powder initially formed on a $Ti_{an, 3\ min}$ catalyst

(1.45 mg). Interestingly, while dissolution of the Ti_{an} catalysts could be lowered at higher electrolyte pH (pH 4.5 and 5.8, adjusted using KOH), the amount of CH_3OH formed decreased significantly. This suggests that the active species for FAR to CH_3OH is HCOOH, rather than $HCOO^-$ (pK_a of HCOOH = 3.6-3.8).[32]

To close this section, we note that FAR to CH_3OH cannot be extended to other metal electrodes, even if they have been anodized (Table S10). This is exemplified using Sn and Cr electrodes, which were previously reported to exhibit FAR activity.[15,16] At –1.0 V, no CH_3OH was detected from both polished and anodised Sn discs, while insignificant amounts of CH_3OH were observed on a polished Cr disc (FE_{CH3OH} of 0.07 %, j_{CH3OH} of –0.08 mA/cm^2) and anodised Cr (FE_{CH3OH} of 0.005 %, j_{CH3OH} of –0.007 mA/cm^2).

2.3. Identification of the active sites for FAR to CH₃OH

In this section, we evaluate our proposition that TOVs are the active sites for FAR to CH_3OH. The paramagnetic TOVs in the Ti_{an} samples can be quantified using electron paramagnetic resonance (EPR) spectroscopy.[33] Ti discs were first anodised at +0.25 A/cm^2 in 0.2 M KCl solution for 1, 2, 3 and 4 min, respectively, and then used for FAR. Three discs were studied at each anodisation time. The Ti_{an} layers were removed from the discs for EPR analysis.

The EPR spectra of the Ti_{an} catalysts before and after FAR are shown in Figure 3a. Before FAR, no EPR signals from Ti^{3+} or OVs were observed. After 60 min FAR at –1.0 V, the Ti_{an} samples exhibited a broad EPR signal at g = 1.94 which can be assigned to paramagnetic Ti^{3+} centres trapped on defects in amorphous titania.[34,35] The peak at g = 2.003 is attributed to the presence of OVs.[36] Since Ti^{3+} and OVs are concurrently formed, we shall use both their EPR signals to quantify the TOVs present.

We found that when the anodisation time of the Ti foil was increased from 1 to 4 min, the mass of Ti_{an} powder formed and EPR signal for the TOVs increased by ~5 times (Figure 3b, Table S11). More importantly, we observed a positive correlation between the amount of TOVs and j_{CH3OH}: extending the anodisation times for the Ti_{an} catalyst from 1 to 4 min increased the amount of TOVs on the catalyst by ~5 times, which led to a 2.5× higher j_{CH3OH} from FAR (Figure 3c). However, the mass-normalised EPR signal areas of the TOVs are relatively constant across all anodisation times, which indicates that the quantity of TOVs present per unit mass of Ti_{an} catalyst is similar (Figure 3b).

We also recorded cyclic voltammograms of the Ti_{an} samples after FAR at −1.0 V to determine if the TOVs are accessible for electrolysis (Figure 3d). The broad oxidation peak observed from −0.85 to 1.35 V can be assigned to the oxidation of the TOVs to Ti^{4+}.[37] The population of TOVs on the catalysts can be estimated using the integrated charges in this peak (Figure 3e, Table S12), and were also found to be positively correlated with j_{CH3OH} (Figure 3f). This complements the findings from the EPR analysis. Overall, our EPR and CV results show that the amount of TOVs is correlated to CH_3OH production. Assuming that all available TOVs on a $Ti_{an, 3 min}$ catalyst are active, the average turnover frequency (TOF) of CH_3OH formation at −1.0 V was determined to be 8.5×10^{-4} s^{-1} (Section S7.2).

We also performed experiments on crystalline anatase and rutile TiO_2 samples (0.15–1 µm in particle size) drop-casted on a Ti disc at −1.0 V (Section S4.3, Figure S3). No TOVs were observed from the voltammograms of rutile and anatase TiO_2 particles after FAR. Interestingly, these catalysts reduce HCOOH to CH_3OH with a FE_{CH3OH} of < 0.2 % and j_{CH3OH} of −0.05 mA/cm^2. These observations further verify the role of TOVs as active sites for FAR to CH_3OH.
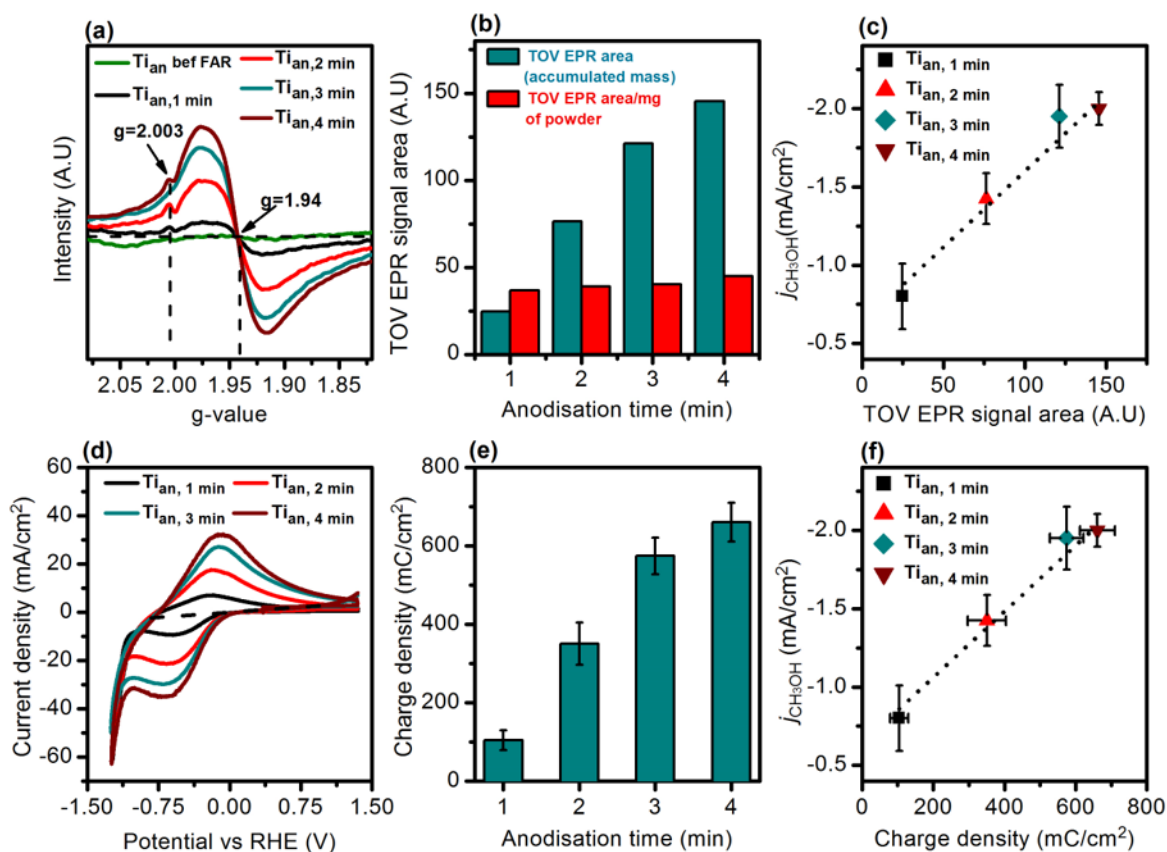
Figure 3. (a) EPR spectra of Ti$_{an}$ samples (anodised over 1, 2, 3 and 4 min) after they were used as catalysts for 60 min FAR at –1.0 V vs RHE. The catalyst before FAR had been anodised for 3 min. (b) EPR signal areas of TOVs on Ti$_{an}$ samples (anodised for 1, 2, 3 and 4 min) (dark cyan bar) and EPR signal areas normalized to mass of Ti$_{an}$ samples (red bar). (c) Dependence of j_{CH3OH} on the amount of TOVs, based on EPR signal areas (dotted lines are included to guide the eye). (d) Cyclic voltammograms (cathodic sweep first) of the Ti$_{an}$ samples after 60 min FAR at –1.0 V vs RHE. Scan rate: 50 mV/s. The electrolyte used was 0.1 M K$_2$SO$_4$ + 0.5 M HCOOH. (e) Anodic peak areas (mC/cm^2; from –0.85 to 1.35 V vs RHE) corresponding to the amount of TOVs on the Ti$_{an}$ samples (anodised over 1, 2, 3 and 4 min). (f) Dependence of j_{CH3OH} on the amount of TOVs, based on anodic peak areas (dotted lines are included to guide the eye).

Additionally, we note that Ti$_{an}$ catalysts anodised for longer times exhibited poorer selectivity for the HER; for example, the FEs for H$_2$ decreased from 87 % on Ti$_{an, 1 \, min}$ to 70 % on Ti$_{an, 4 \, min}$ (Table S14). Thus, to sum up, increasing the number of TOV sites in Ti$_{an}$ improves the selectivity for CH$_3$OH from FAR, while suppressing the competing HER.

2.4. Mechanistic pathway for FAR to CH$_3$OH

We will now interplay theory and experiments to probe the role of TOVs as active sites and elucidate the FAR reaction pathway to CH$_3$OH. We first modelled the most stable bulk structure of TiO$_2$, i.e., the rutile phase. After optimizing its geometry, we modelled its most

stable surface termination, $TiO_2(110)$. This surface has alternating rows of coordinatively unsaturated (CUS) and bridge sites (Figure 4a). CUS sites have undercoordinated Ti atoms available for interacting with the adsorbates, while bridge sites do not. Conversely, bridge sites have twofold-coordinated oxygen atoms (O_{2c}), which are known to leave TOVs on TiO_2.[38] To incorporate the heterogeneity of amorphous Ti_{an} as observed from our XRD and Raman experiments, we also modelled two stepped surfaces: CUS-terminated $TiO_2(120)$ (denoted $TiO_2(120)$-CT) and bridge-terminated $TiO_2(120)$ (denoted $TiO_2(120)$-BT). These surfaces have alternating rows of CUS and bridge sites (with their corresponding O_{2c}), and a unique type of O_{2c} located at edge sites (denoted E-O_{2c}).
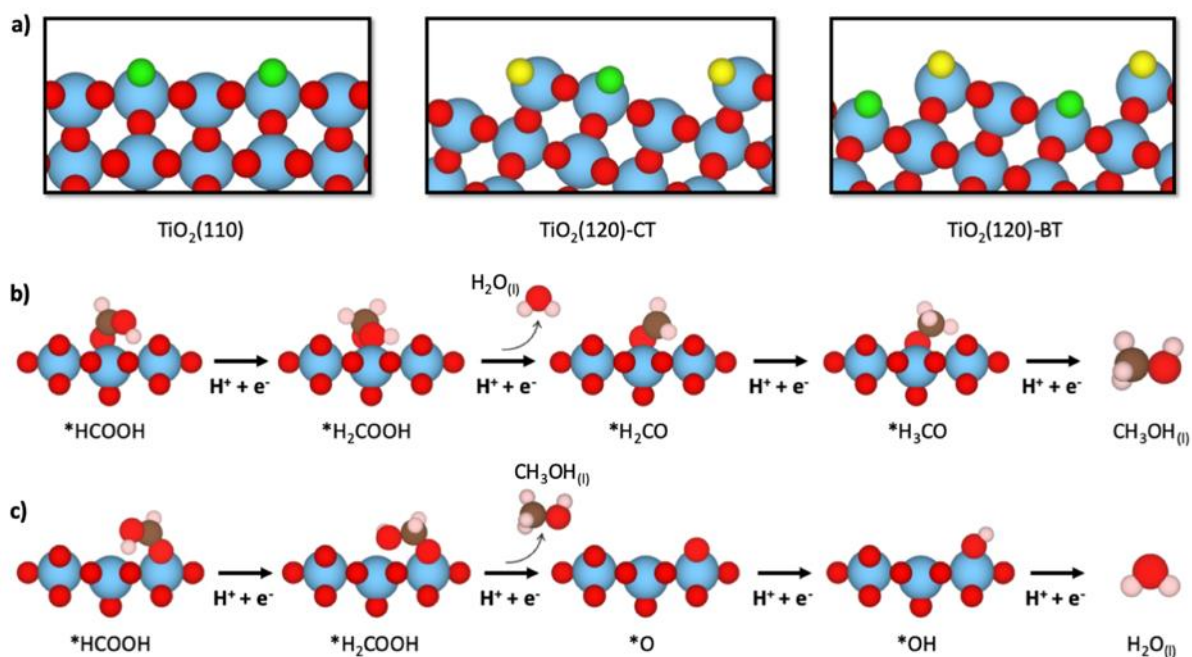

Figure 4. (a) Schematics of the slab models used in this work. Ti atoms are shown in blue, O in red, bridge site oxygen atoms (O_{2c}) in green, and edge site oxygen atoms (E-O_{2c}) in yellow. The lowest-energy pathway for FAR to CH_3OH at (b) CUS sites and (c) on TOVs. In (b) and (c), the Ti, O, C, and H atoms are shown in blue, red, brown, and pink, respectively.

To determine if TOVs could be formed on the stepped TiO_2 surfaces, we calculated the oxygen vacancy formation energies ($\Delta E_{TOV} = E_{slab-TOV} + \frac{1}{2}E_{O2} - E_{slab}$, where $E_{slab-TOV}$ is the energy of the slab with an oxygen vacancy, E_{O2} is the corrected total energy of gas-phase molecular oxygen, and E_{slab} is the energy of the pristine slab). Values of 3.04 and 2.93 eV were obtained for O_{2c} at $TiO_2(120)$-CT and $TiO_2(120)$-BT, respectively, while on $TiO_2(110)$, it is

3.75 eV. These results lead us to conclude that TOVs are more facilely formed on stepped TiO$_2$ surfaces. This is in line with our experimental results, where the formation of TOVs was observed on amorphous Ti$_{an}$, but not on highly crystalline rutile and anatase TiO$_2$ particles (Section S4.3). Furthermore, the values of ΔE_{TOV} for E-O$_{2c}$ were found to be around 0.3 eV more unstable in both cases, indicating that TOVs are more favourably formed on O$_{2c}$, rather than E-O$_{2c}$, on these surfaces.

Next, we determined the most favorable pathway for FAR to CH$_3$OH on CUS sites and TOVs (Tables S15 and S16, Figures S12-S17). On both sites, the hydrogenation of *HCOOH results in the formation of *H$_2$COOH, but the pathways bifurcate from that point on. On CUS sites, *H$_2$COOH is hydrogenated to produce *H$_2$CO + H$_2$O$_{(l)}$ (Figure 4b; note that *H$_2$CO is adsorbed formaldehyde). This is similar to a previously proposed mechanism for FAR to CH$_3$OH on Cr, where *H$_2$COOH is initially formed and splits into *CHO + H$_2$O, and *CHO then undergoes hydrogenation to form CH$_3$OH via a *H$_2$CO intermediate.[16] In contrast, on the TOVs, the protonation of *H$_2$COOH results in the direct formation of CH$_3$OH and the filling of the TOV with *O (Figure 4c).

Free-energy diagrams for FAR on the different surface sites were made to facilitate the quantitative analysis of both pathways (Figure 5a). The pathways at CUS sites (denoted as TiO$_2$(110), TiO$_2$(120)-CT and TiO$_2$(120)-BT) show that the hydrogenation of HCOOH to *H$_2$COOH is the potential-limiting step. The calculated onset potentials are –1.27, –1.57, and –1.21 V at CUS sites for TiO$_2$(110), TiO$_2$(120)-CT and TiO$_2$(120)-BT, respectively. In contrast, the reduction of HCOOH on TOVs (denoted TiO$_2$(110)-O, TiO$_2$(120)-CT-O, and TiO$_2$(120)-BT-O) proceeds via the exothermic formation of *H$_2$COOH. The potential-limiting step is the protonation of *OH to form H$_2$O$_{(l)}$, which regenerates the TOV and restarts the catalytic cycle. The onset potentials are –1.17, –0.77, and –0.54 V for TiO$_2$(110)-O, TiO$_2$(120)-CT-O, and TiO$_2$(120)-BT-O, respectively. Clearly, the onset potentials at TOVs are considerably lower

than those at CUS sites, which can be attributed to the favourable formation of *H_2COOH and

the opening of a different catalytic pathway. These results highlight two key findings: (i) based

on their lower onset potentials, we identify TOVs at steps as the most active sites for FAR to

CH_3OH, and (ii) adsorbed formaldehyde (*H_2CO) is not part of the FAR reaction pathway on

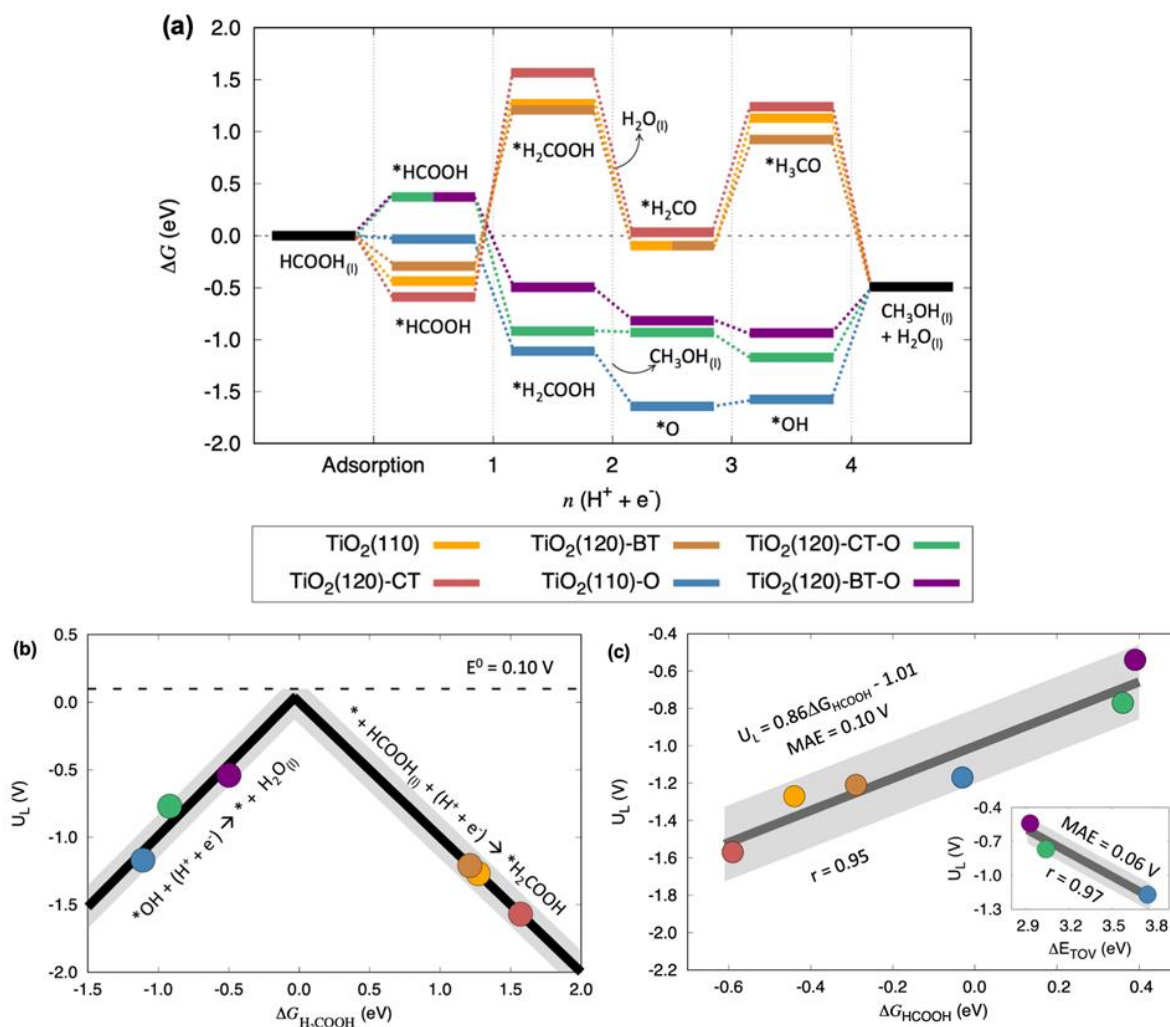TOVs, but is a key intermediate during FAR on CUS sites.

Figure 5. (a) Free-energy diagrams at 0 V vs RHE for FAR to CH_3OH at CUS and TOV sites. The intermediates and active sites are shown in Figure 4. (b) Volcano plot correlating the onset potential for FAR with the adsorption energy of *H_2COOH. The dashed line corresponds to the calculated equilibrium potential (0.10 V vs RHE, it is 0.11 V vs RHE in experiments). Gray bands of $\pm$ 0.16 V around the black lines correspond to $\pm$ 2MAE (MAE: mean absolute error) of the scaling relation between *H_2COOH and *OH. (c) Calculated onset potential as a function of the adsorption free energy of formic acid. The MAE and the Pearson regression coefficient (r) are also provided together with a linear regression in dark grey and a light grey zone of $\pm$ 2MAE. Inset: Calculated onset potential as a function of the oxygen vacancy formation energy at TOV sites. The color code for each active site is the same in all panels and is shown at the center of the figure.

14

We also determine if the sizable difference of FAR activities between CUS sites and TOVs could be observed on anatase TiO_2. A similar conclusion was obtained: the calculated onset potentials were -1.75 and -0.58 V on anatase $TiO_2(101)$ without and with TOVs, respectively (denoted A-$TiO_2(101)$ and A-$TiO_2(101)$-O, Tables S15-S16, Figures S18-S19), which reaffirms our findings that TOVs on TiO_2 are the active sites for CH_3OH production.

Figure 5b condenses the activity trends in a Sabatier-type activity plot, using the adsorption energy of $*H_2COOH$ (ΔG_{H2COOH}) as a descriptor. CUS sites are on the weak-binding (right) leg of the volcano, where the formation of $*H_2COOH$ is potential-limiting. TOVs are on the strong-binding (left) leg, where $*OH$ hydrogenation is potential-limiting. We found that the onset potential (U_L) at the peak lies close to the equilibrium potential (E_0) when $\Delta G_{H2COOH} \approx 0$. This indicates that: (i) it is thermodynamically feasible to synthesise nearly ideal FAR electrocatalysts, (ii) $\Delta G_{H2COOH} \approx 0$ is a simple guiding principle for the computational selection of promising FAR catalysts. Accordingly, optimal catalysts for FAR should feature a free energy of adsorption close to 0 eV for $*H_2COOH$.

In the search for complementary guiding principles, we found that the free energy of adsorption of HCOOH can also be used as a descriptor for FAR activity: the weaker the binding energy of $*HCOOH$, the more positive the U_L (Figure 5c). This descriptor is useful because the adsorption energy of HCOOH can be calculated with DFT and/or measured experimentally.[39,40] The correlation in Figure 5c shows that HCOOH adsorbs strongly on CUS sites and weakly on TOVs, and that the opposite is true for the next intermediate, $*H_2COOH$. Thus, weakly bound $*H_2COOH$ on CUS sites is reduced to CH_3OH through a high-overpotential pathway, while strongly bound $*H_2COOH$ on TOVs reduces to CH_3OH via a low-overpotential pathway (Figure 5a). We note, however, that the correlation in Figure 5c is to be taken with caution, because if the $*HCOOH$ adsorption energy is too weak, it might not adsorb at all, and no activity will be observed.

Additionally, we find that ΔE_{TOV} is inversely correlated with U_L (inset of Figure 5c). Hence, surface sites with more positive TOV formation energies have simultaneously more stable *OH adsorption energies. This is justified by the following facts: (i) ΔE_{TOV} is the additive inverse of the oxygen adsorption energy at the vacancy ($\Delta E_O = - \Delta E_{TOV}$), (ii) *OH and *O adsorption energies are linearly related by the so-called scaling relations,[18] and (iii) $U_L = \Delta G_{OH}$ on TOVs, since *OH hydrogenation is the potential-limiting step of FAR to CH_3OH. Therefore, TOV formation energies may be used as a quantitative criterion for the design of FAR catalysts.

We further found that *H is more weakly bound on TOVs than on CUS sites (Tables S15-S16). Since TiO_2 lies on the weak binding arm in the Sabatier plot for HER,[41] weakening *H on TOVs should lead to a poor HER activity on Ti_{an}, in excellent agreement with our experimental observations. Interestingly, the adsorption free energy of *H scales linearly with that of *HCOOH (Figure S10). Therefore, we expect a higher FAR activity and lower *H coverage (or poorer HER) when *HCOOH is weakly adsorbed on the surface.

We now use experiments to assess the reaction pathway predicted by the computational analysis (shown in Figure 5a). Based on our calculations, CH_2O is not an intermediate species during FAR to CH_3OH on TOVs. We verify this experimentally by performing HCOOH and CH_2O spike tests on $Ti_{an, 3 min}$ during chronoamperometry at –1.0 V (Figure 6a). While the HCOOH spike (0.1 M K_2SO_4 + 5 mM HCOOH, pH 3.5) generated higher current densities, CH_2O (0.1 M K_2SO_4 + 5 mM CH_2O; adjusted with H_2SO_4 to pH 3.5) was electrochemically inert. We further electrolysed 5 mM CH_2O (nominal concentration) on a $Ti_{an, 3 min}$ catalyst at potentials from –0.95 V to –1.05 V (Table S17). Interestingly, we detected similar amounts of CH_3OH and HCOOH at all potentials. For example, we detected 0.08 mM of CH_3OH and 0.09 mM of HCOOH, after CH_2O electrolysis at –1.0 V (Figure 6b, Tables S17-S18, Section S7.3). This strongly suggests that the CH_3OH observed was formed through the Cannizzaro disproportionation reaction of CH_2O ($2CH_2O + OH^- \rightarrow HCOO^- + CH_3OH$), rather than via an

electrocatalytic reduction.[42] The electrochemical inertness of CH_2O on the $Ti_{an,\ 3\ min}$ catalyst also allows us to rule out CUS sites as the active sites.

Lastly, CO and CO_2 might be possible intermediates for FAR to CH_3OH.[43] However, we did not detect CH_3OH when we reduced CO and CO_2 at -1.0 V in 0.1 M K_2SO_4 (pH adjusted to 2.6 with H_2SO_4) (Table S17). This excludes both molecules as active intermediates.
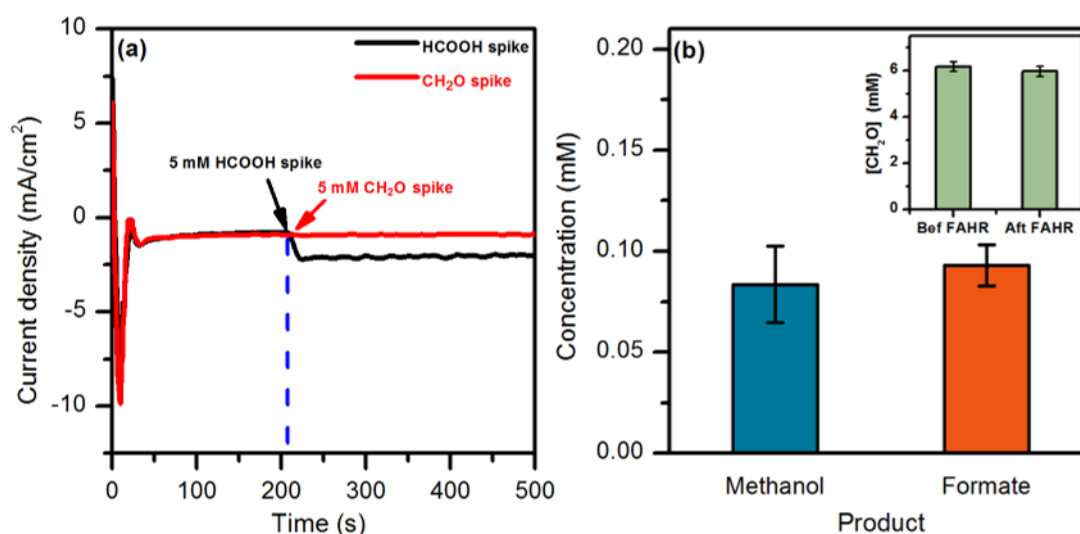

Figure 6. (a) Spike tests of HCOOH (black line) and CH_2O (red line) in 0.1 M K_2SO_4 at -1.0 V vs RHE on a $Ti_{an,\ 3\ min}$ catalyst. (b) CH_3OH and HCOOH concentrations after formaldehyde reduction (FAHR) at -1.0 V vs RHE on a $Ti_{an,\ 3\ min}$ catalyst. The inset graph shows the CH_2O concentrations before and after FAHR at -1.0 V vs RHE, based on UV-Vis measurements using the chromotropic acid method. The increase in CH_3OH and HCOOH concentrations is attributed to the Cannizzaro disproportionation of CH_2O.

Collectively, we have elucidated that strongly reducing TOVs on Ti_{an} are the active sites for FAR to CH_3OH. The mechanistic pathway proceeds through a direct reduction of HCOOH on Ti_{an}, whereas previously recognised intermediates for CH_3OH production, such as *H_2CO, can be ruled out.[16]. Our results show that aliphatic carboxylic acids can be directly electroreduced to alcohols under ambient conditions using only water as the H source. This contrasts with the conventional reduction of carboxylic acids using stoichiometric reagents such as $LiAlH_4$, which leads to a large production of Li and Al waste by-products.[44]

17

3. Conclusions

In this work, we exemplify the use of Ti_{an} for electrocatalytic FAR to CH_3OH. Characterisation studies indicate that the Ti_{an} catalyst is highly amorphous and bears TOV sites during electrocatalytic FAR. The optimum FE_{CH3OH} and j_{CH3OH} obtained for FAR on $Ti_{an, 3\ min}$ samples were 12.6 % and –2 mA/cm^2, respectively. A detailed examination of the Ti_{an} catalyst using EPR spectroscopy and CV indicates that the increase in CH_3OH production is correlated with the amount of TOVs in the catalyst. DFT calculations showed that the most favourable reaction pathway is through the protonation of a $*H_2COOH$ intermediate to produce CH_3OH and $*O$, filling the previously formed vacancy. Subsequent hydrogenation to $*OH$ and $H_2O_{(l)}$ regenerates the TOV, completing the catalytic cycle. In addition, the adsorption energies of $*HCOOH$ and $*H_2COOH$, as well as the formation energy of TOVs can be used as complementary descriptors to guide the design of enhanced FAR catalysts.

In a broader context, our work illustrates how we can rationally design an electrocatalyst for the reduction of a highly stable organic functional group, in this case the carboxylic acid group. By introducing enhanced catalytic sites such as TOVs on anodised Ti, a non-noble, earth-abundant element, the carboxylic acid group can be favourably reduced to produce a valuable alcohol. Apart from showing the feasibility of CH_3OH synthesis under ambient conditions from CO_2 reduction via tandem electrocatalysis, this work provides an alternative route for valorizing longer-chain aliphatic acids to valuable alcohols such as *n*-propanol.

Supporting information

Detailed experimental and theoretical procedures, characterisation methods, gas-phase and liquid-phase corrections, specific free-energy values including ZPE and TS corrections, and the coordinates of the optimized slabs.

Acknowledgements

References

(1) Räuchle, K.; Plass, L.; Wernicke, H. J.; Bertau, M. Methanol for Renewable Energy Storage and Utilization. *Energy Technol.* **2016**, *4* (1), 193–200.

(2) Dalena, F.; Senatore, A.; Marino, A.; Gordano, A.; Basile, M.; Basile, A. Methanol Production and Applications: An Overview. In *Methanol: Science and Engineering*; Basile, A., Dalena, F., Eds.; Elsevier B.V.: Amsterdam, **2018**; pp 3–28.

(3) Ott, J.; Gronemann, V.; Pontzen, F.; Fiedler, E.; Grossmann, G. Methanol. In *Ullmann's Encyclopedia of Industrial Chemistry*; Ullmann, F., Gerhartz, W., Yamamoto, Y. S., Campbell, F. T., Pfefferkorn, R., Rounsaville, J. F., Eds.; Wiley-VCH Verlag GmbH & Co. KGaA: Weinheim, Germany, **2012**; pp 8–9.

(4) Rumayor, M.; Dominguez-Ramos, A.; Irabien, A. Innovative Alternatives to Methanol Manufacture: Carbon Footprint Assessment. *J. Cleaner. Prod.* **2019**, *225*, 426–434.

(5) Hatsukade, T.; Kuhl, K. P.; Cave, E. R.; Abram, D. N.; Feaster, J. T.; Jongerius, A. L.; Hahn, C.; Jaramillo, T. F. Carbon Dioxide Electroreduction Using a Silver–Zinc Alloy. *Energy Technol.* **2017**, *5* (6), 955–961.

(6) Low, Q. H.; Loo, N. W. X.; Calle-Vallejo, F.; Yeo, B. S. Enhanced Electroreduction of Carbon Dioxide to Methanol Using Zinc Dendrites Pulse-Deposited on Silver Foam. *Angew. Chem. Int. Ed.* **2019**, *58* (8), 2256–2260.

(7) He, Y.; Jiang, W. J.; Zhang, Y.; Huang, L. B.; Hu, J. S. Pore-Structure-Directed CO_2 Electroreduction to Formate on SnO_2/C Catalysts. *J. Mater. Chem. A* **2019**, *7* (31), 18428–18433.

(8) White, J. L.; Bocarsly, A. B. Enhanced Carbon Dioxide Reduction Activity on Indium-Based Nanoparticles. *J. Electrochem. Soc.* **2016**, *163* (6), H410–H416.

(9)   Pander, J. E.; Lum, J. W. J.; Yeo, B. S. The Importance of Morphology on the Activity of Lead Cathodes for the Reduction of Carbon Dioxide to Formate. *J. Mater. Chem. A* **2019**, *7* (8), 4093–4101.

(10)   Dean, J. A. Section 6: Thermodynamic Properties. In *Lange's Handbook of Chemistry.*; Dean, J. A., Lange, N. A., Eds.; McGraw-Hill: Knoxville, **1999**; pp 6.1-6.147.

(11)   Sadakiyo, M.; Hata, S.; Fukushima, T.; Juhász, G.; Yamauchi, M. Electrochemical Hydrogenation of Non-Aromatic Carboxylic Acid Derivatives as a Sustainable Synthesis Process: From Catalyst Design to Device Construction. *Phys. Chem. Chem. Phys.* **2019**, *21* (11), 5882–5889.

(12)   Bondue, C. J.; Calle-Vallejo, F.; Figueiredo, M. C.; Koper, M. T. M. Structural Principles to Steer the Selectivity of the Electrocatalytic Reduction of Aliphatic Ketones on Platinum. *Nat. Catal.* **2019**, *2* (3), 243–250.

(13)   Ledezma-Yanez, I.; Gallent, E. P.; Koper, M. T. M.; Calle-Vallejo, F. Structure-Sensitive Electroreduction of Acetaldehyde to Ethanol on Copper and Its Mechanistic Implications for CO and CO_2 Reduction. *Catal. Today* **2016**, *262*, 90–94.

(14)   Schouten, K. J. P.; Kwon, Y.; Van Der Ham, C. J. M.; Qin, Z.; Koper, M. T. M. A New Mechanism for the Selectivity to C_1 and C_2 Species in the Electrochemical Reduction of Carbon Dioxide on Copper Electrodes. *Chem. Sci.* **2011**, *2* (10), 1902–1909.

(15)   Russell, P. G.; Kovac.N; Srinivasan.S; Steinberg.M. The Electrochemical Reduction of Carbon Dioxide, Formic Acid, and Formaldehyde. *J. Electrochem. Soc.* **1977**, *124* (9), 1329–1338.

(16)   Kotoulas, I.; Kyriacou, G. Conversion of Carbon Dioxide to Methanol through the Reduction of Formic Acid on Chromium. *J. Chem. Technol. Biotechnol.* **2017**, *92* (7), 1794–1800.

(17)   Adegoke, K. A.; Radhakrishnan, S. G.; Gray, C. L.; Sowa, B.; Morais, C.; Rayess, P.; Rohwer, E. R.; Comminges, C.; Kokoh, K. B.; Roduner, E. Highly Efficient Formic Acid and Carbon Dioxide Electro-Reduction to Alcohols on Indium Oxide Electrodes. *Sustainable Energy Fuels* **2020**, *4* (8), 4030–4038.

(18)   Su, H. Y.; Ma, X.; Sun, K.; Sun, C.; Xu, Y.; Calle-Vallejo, F. Trends in C-O and N-O Bond Scission on Rutile Oxides Described Using Oxygen Vacancy Formation Energies. *Chem. Sci.* **2020**, *11* (16), 4119–4124.

(19)   Zhou, Y.; Chen, C.; Wang, N.; Li, Y.; Ding, H. Stable Ti^{3+} Self-Doped Anatase-Rutile Mixed TiO_2 with Enhanced Visible Light Utilization and Durability. *J. Phys. Chem. C* **2016**, *120* (11), 6116–6124.

(20)   Walle, L. E.; Borg, A.; Johansson, E. M. J.; Plogmaker, S.; Rensmo, H.; Uvdal, P.; Sandell, A. Mixed Dissociative and Molecular Water Adsorption on Anatase TiO_2(101). *J. Phys. Chem. C* **2011**, *115* (19), 9545–9550.

(21)   Syres, K. L.; Thomas, A. G.; Flavell, W. R.; Spencer, B. F.; Bondino, F.; Malvestuto, M.; Preobrajenski, A.; Grätzel, M. Adsorbate-Induced Modification of Surface Electronic Structure: Pyrocatechol Adsorption on the Anatase TiO_2 (101) and Rutile TiO_2 (110) Surfaces. *J. Phys. Chem. C* **2012**, *116* (44), 23515–23525.

(22) Wierzbicka, E.; Zhou, X.; Denisov, N.; Yoo, J. E.; Fehn, D.; Liu, N.; Meyer, K.; Schmuki, P. Self-Enhancing H_2 Evolution from TiO_2 Nanostructures under Illumination. *ChemSusChem* **2019**, *12* (9), 1900–1905.

(23) Zhang, Z.; Hedhili, M. N.; Zhu, H.; Wang, P. Electrochemical Reduction Induced Self-Doping of Ti^{3+} for Efficient Water Splitting Performance on TiO_2 Based Photoelectrodes. *Phys. Chem. Chem. Phys.* **2013**, *15* (37), 15637–15644.

(24) Balachandran, U.; Eror, N. G. Raman Spectra of Titanium Dioxide. *J. Solid State Chem.* **1982**, *42* (3), 276–282.

(25) Yanagisawa, K.; Ovenstone, J. Crystallization of Anatase from Amorphous Titania Using the Hydrothermal Technique: Effects of Starting Material and Temperature. *J. Phys. Chem. B* **1999**, *103* (37), 7781–7787.

(26) Zhang, G.; Huang, C.; Zhou, L.; Ye, L.; Huang, H. Enhanced Charge Storage by the Electrocatalytic Effect of Anodic TiO_2 Nanotubes. *Nanoscale* **2011**, *3*, 4174–4181.

(27) Aijo, J. K.; Thankamoniamma, M.; Puigdollers, J.; Anuroop, R.; Pradeep, B.; Shripathi, T.; Philip, R. R. Rapid Room Temperature Crystallization of TiO_2 Nanotubes. *CrystEngComm* **2017**, *19* (12), 1585–1589.

(28) Nair, S. B.; Aijo, J. K.; Menon, S. S.; Rahman, H.; Joseph, J. A.; Shaji, S.; Philip, R. R. Influence of Electrochemical Reduction of Selfdoping on the Low Temperature Crystallization and Photocatalytic Activities of TiO_2 Nanotubes. *Semicond. Sci. Technol.* **2019**, *34* (9), 095023.

(29) Morikawa, Y.; Takahashi, I.; Aizawa, M.; Namai, Y.; Sasaki, T.; Iwasawa, Y. First-Principles Theoretical Study and Scanning Tunneling Microscopic Observation of Dehydration Process of Formic Acid on a $TiO_2(110)$ Surface. *J. Phys. Chem. B* **2004**, *108* (38), 14446–14451.

(30) Aizawa, M.; Morikawa, Y.; Namai, Y.; Morikawa, H.; Iwasawa, Y. Oxygen Vacancy Promoting Catalytic Dehydration of Formic Acid on $TiO_2(110)$ by in situ Scanning Tunneling Microscopic Observation. *J. Phys. Chem. B* **2005**, *109* (40), 18831–18838.

(31) McCafferty, E. Thermodynamics of Corrosion: Pourbaix Diagrams. In *Introduction to Corrosion Science*; Springer: Washington, **2010**; p 110.

(32) Wang, X.; Fu, H.; Du, D.; Zhou, Z.; Zhang, A.; Su, C.; Ma, K. The Comparison of pKa Determination between Carbonic Acid and Formic Acid and Its Application to Prediction of the Hydration Numbers. *Chem. Phys. Lett.* **2008**, *460* (1–3), 339–342.

(33) Fu, G.; Zhou, P.; Zhao, M.; Zhu, W.; Yan, S.; Yu, T.; Zou, Z. Carbon Coating Stabilized Ti^{3+}-Doped TiO_2 for Photocatalytic Hydrogen Generation under Visible Light Irradiation. *Dalton Trans.* **2015**, *44* (28), 12812–12817.

(34) Wierzbicka, E.; Osuagwu, B.; Denisov, N.; Fehn, D.; Meyer, K.; Schmuki, P. Light-Induced in-situ Ti^{3+} Formation in TiO_2 Nanosheets for Photocatalytic Hydrogen Evolution. *IOP Conf. Ser. : Mater. Sci. Eng.* **2020**, *908* (1), 012001.

(35) Chiesa, M.; Paganini, M. C.; Livraghi, S.; Giamello, E. Charge Trapping in TiO_2 Polymorphs as Seen by Electron Paramagnetic Resonance Spectroscopy. *Phys. Chem. Chem. Phys.* **2013**, *15* (24), 9435–9447.

(36) Sarkar, A.; Khan, G. G. The Formation and Detection Techniques of Oxygen

Vacancies in Titanium Oxide-Based Nanostructures. *Nanoscale* **2019**, *11* (8), 3414–3444.

(37)   Ghicov, A.; Tsuchiya, H.; Hahn, R.; MacAk, J. M.; Muñoz, A. G.; Schmuki, P. TiO_2 Nanotubes: H^+ Insertion and Strong Electrochromic Effects. *Electrochem. Commun.* **2006**, *8* (4), 528–532.

(38)   Yamamoto, Y.; Kasamatsu, S.; Sugino, O. Scaling Relation of Oxygen Reduction Reaction Intermediates at Defective TiO_2 Surfaces. *J. Phys. Chem. C* **2019**, *123* (32), 19486–19492.

(39)   Campbell, C. T.; Sellers, J. R. V. Enthalpies and Entropies of Adsorption on Well-Defined Oxide Surfaces: Experimental Measurements. *Chem. Rev.* **2013**, *113* (6), 4106–4135.

(40)   Rumptz, J. R.; Campbell, C. T. Adhesion Energies of Solvent Films to Pt(111) and Ni(111) Surfaces by Adsorption Calorimetry. *ACS Catal.* **2019**, No. 111, 11819–11825.

(41)   Laursen, A. B.; Varela, A. S.; Dionigi, F.; Fanchiu, H.; Miller, C.; Trinhammer, O. L.; Rossmeisl, J.; Dahl, S. Electrochemical Hydrogen Evolution: Sabatier's Principle and the Volcano Plot. *J. Chem. Educ.* **2012**, *89* (12), 1595–1599.

(42)   Birdja, Y. Y.; Koper, M. T. M. The Importance of Cannizzaro-Type Reactions during Electrocatalytic Reduction of Carbon Dioxide. *J. Am. Chem. Soc.* **2017**, *139* (5), 2030–2034.

(43)   Schizodimou, A.; Kotoulas, I.; Kyriacou, G. Electrochemical Reduction of Formic Acid through Its Decarbonylation in Phosphoric Acid Solution. *Electrochim. Acta* **2016**, *210*, 236–239.

(44)   Harinath, A.; Bhattacharjee, J.; Panda, T. K. Facile Reduction of Carboxylic Acids to Primary Alcohols under Catalyst-Free and Solvent-Free Conditions. *Chem. Commun.* **2019**, *55* (10), 1386–1389.

For Table of Contents only